MATERIALS SCIENCE

Wireless graphene-based thermal patch for obtaining temperature distribution and performing thermography

Minpyo Kang[1]†, Hyerin Jeong[2]†, Sung-Won Park[2], Juyeong Hong[1], Hyeyeon Lee[1], Youngcheol Chae[1]*, Sunggu Yang[2]*, Jong-Hyun Ahn[1]*

Thermal imaging provides information regarding the general condition of the human body and facilitates the diagnosis of various diseases. Heat therapy or thermotherapy can help in the treatment of injuries to the skin tissue. Here, we report a wearable thermal patch with dual functions of continuous skin temperature sensing and thermotherapy for effective self-care treatment. This system consists of a graphene-based capacitive sensor, a graphene thermal pad, and a flexible readout board with a wireless communication module. The wearable sensor continuously monitors the temperature variation over a large area of the skin ($3 \times 3 cm^2$) with high resolution and sensitivity and performs thermotherapy via the graphene-based heater mounted at the bottom of the device. Animal studies prove that the proposed system can be used to diagnose various diseases. This technology could be useful in the development of convenient and wearable health care devices.

INTRODUCTION

The human body temperature, which is the result of physical activity and metabolism, is an important parameter for the noninvasive prediction of various diseases and physical conditions (*1*, *2*). Temperature distribution of human skin, which aids in the diagnosis and treatment of various medical conditions, can be obtained by thermal imaging using an infrared (IR) camera. However, this thermography technique requires bulky equipment, which limits continuous monitoring and precise measurement at high resolutions. In addition, IR imaging is indirect and dependent on the thermal radiation of human skin (*3*). Therefore, detection error may occur depending on the condition of the atmosphere or the skin. Commercial IR cameras offer a lack of accuracy with 2°C or 2% discrepancy. An alternative method is therefore required for an accurate measurement. To overcome these problems, thermography can be performed using wearable electronic devices, which are portable and highly accurate, with real-time monitoring for long periods (*4*–*7*). This idea opens unexplored avenues for the advancement of existing thermographic technology.

Several researchers have developed wearable temperature sensors. In most of these studies, the temperature was obtained at a single point (*8*–*12*). For example, Han *et al.* (*8*) developed a wearable temperature sensor that offered the single-pixel temperature measurement from the attached skin. Several sensors attached to target body parts and facilitated real-time monitoring of temperature changes in the body parts. However, these sensors cannot detect skin diseases that require the measurement of temperature gradient over a large area, such as skin bruises and tumors. To detect these complications, the local temperature changes in a desired skin area must be clearly analyzed through high-resolution temperature mapping. The wearable temperature sensors developed for this purpose require both high resolution and high sensitivity (*13*–*17*).

In addition to temperature monitoring, thermotherapy is an important function for wearable health care devices (*18*, *19*). Thermotherapy uses heat to reduce muscle pain and reproduce injured tissues (*20*). The increase in the skin temperature enhances blood flow due to vasodilation, which coincides with increased metabolic rate and tissue extensibility, thereby accelerating the process of tissue healing (*21*, *22*). A thermotherapeutic heater in combination with a thermal sensor array can be used as an alternative to chemical or plugged-in heating pads. However, the clinical benefits have not been confirmed.

In this study, we present a multifunctional, wearable thermal patch composed of a capacitive temperature sensor array (8 by 8) that uses chemical vapor deposition (CVD)–grown graphene (*23*–*25*) for the top and bottom electrodes, as well as a graphene-based heater for thermotherapy, which is installed under the temperature sensor array. The wearable device is integrated with a wireless system and rechargeable battery. The device exhibits targeted, stable performances for temperature monitoring and thermal therapy on a large specific skin area.

RESULTS

Figure 1A shows the schematic image of the wearable thermal patch and its functions. The device consisted of an array of temperature sensors and a heater that are integrated on a medical patch (thickness, 20 μm). Furthermore, it consisted of readout circuits for processing and transmitting the measured data to an external device, such as a smartphone. The temperature map measured on the large skin area (~3 cm by 3 cm) was transferred wirelessly to a smartphone, and the user could precisely control the temperature of the thermotherapy heater with the smartphone. The wearable system has three functions as follows: First of all, a temperature sensor array was used to monitor the temperature distribution and thermal gradient, facilitating the diagnosis of the type and progression of the disease. In addition, a monitoring system was attached to the body, and the body temperature was measured over a long period of time.

[1]School of Electrical and Electronic Engineering, Yonsei University, Seoul 03722, Republic of Korea. [2]Department of Nano-Bioengineering, Incheon National University, Incheon 22012, Republic of Korea.
*Corresponding author. Email: ychae@yonsei.ac.kr (Y.C.); sungguyang@inu.ac.kr (S.Y.); ahnj@yonsei.ac.kr (J.-H. A.)
†These authors contributed equally to this work.

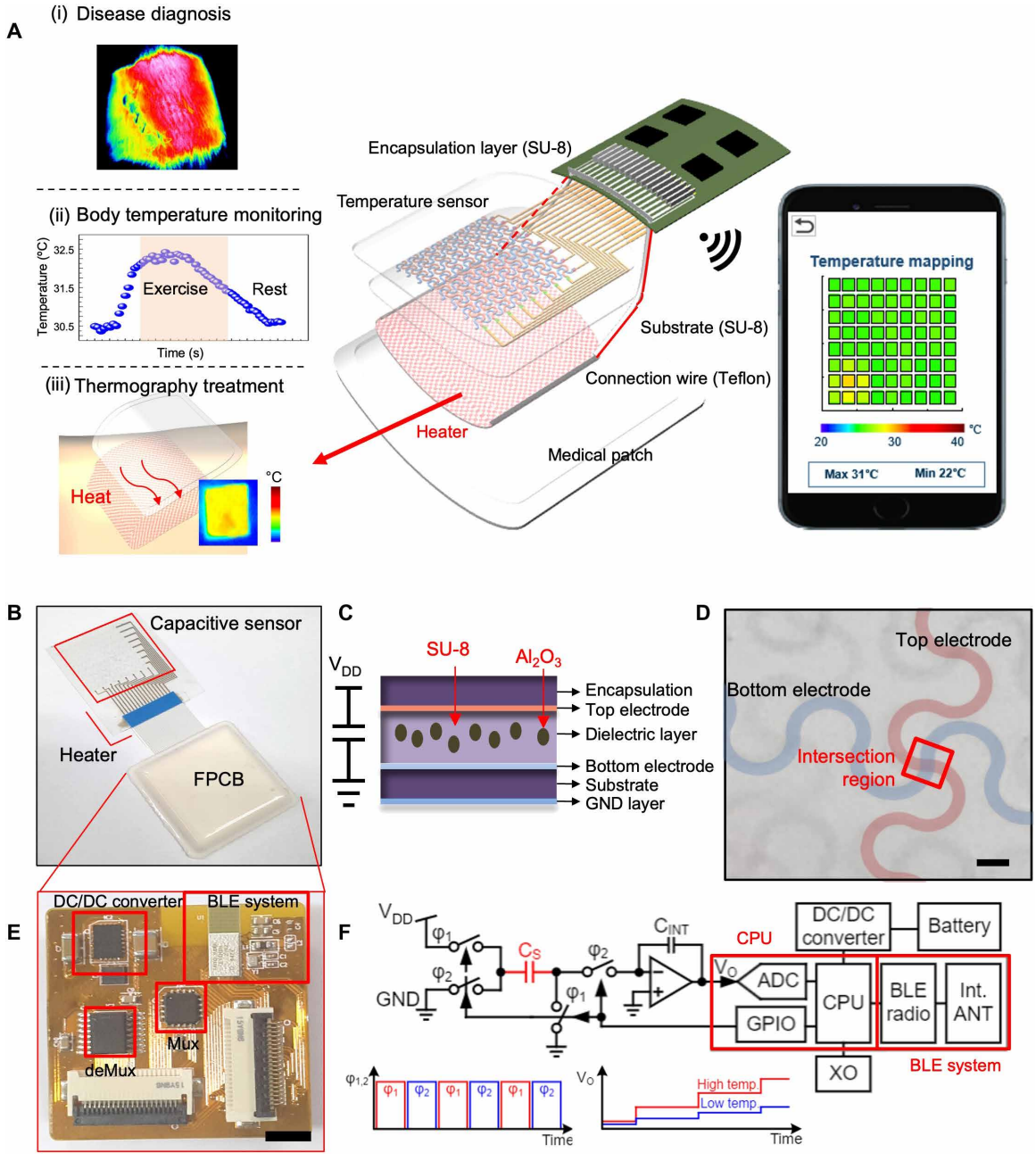

Fig. 1. Biomedical patch for temperature monitoring and heating. (**A**) Functional illustration of the temperature monitoring system. (**B**) Photograph of 8 by 8 array capacitive sensor system. Scale bar, 1 cm. (**C**) Cross-sectional view of the capacitive sensor structure. [encapsulation: SU-8, 2 μm; top and bottom electrodes: two-layer graphene; dielectric layer: SU-8/Al_2O_3 composite 1.5 μm; substrate: SU-8 3 μm; and ground (GND): three-layer graphene]. (**D**) Enlarged image of the capacitive sensor. The red box indicates the region where the top and bottom electrodes intersect. Scale bar, 500 μm. (**E**) Optical image and functional explanation of flexible board. Scale bar, 5 mm. Mux, Multiplexer; deMux, Demultiplexer; GPIO, General Purpose Input/Output; Int. ANT, Internal Antenna. (**F**) Block-diagram for wireless measurement and heating system. The two states are operated alternately to accurately measure capacitance. C_S and C_{INT} indicate capacitance of sensor and internal capacitance in microprocessor, respectively.

The state of the human body could be determined by analyzing the changes in the body temperature that occurred during physical activities, such as exercise and sleep. Furthermore, sleep disorders could be diagnosed by measuring body temperature, which is associated with the sleep stages. Moreover, the system can perform thermography (heat treatment) using a heater located under the sensor array. This system can be used for various medical applications through the use of heat treatment that accelerates wound healing, such as skin diseases.

The overall system consists of three parts: a capacitive temperature sensor, a heater, and a flexible printed circuit board (FPCB) (Fig. 1B). The capacitive temperature sensor of the 8 by 8 array with the pixel space of 2.4 mm was fabricated using four-layer CVD-grown graphene and a composite of SU-8 epoxy and Al_2O_3 particles

for the electrodes and dielectric layer, respectively (Fig. 1C and fig. S1). Graphene offers excellent mechanical flexibility, high optical transmittance, and good biocompatibility, which are required for wearable applications. The SU-8/Al_2O_3 composite (used for the dielectric) was used to complement the undesirable properties of each material: the low dielectric constant of SU-8 and poor mechanical properties of Al_2O_3. Three composites with 5, 10, and 15 weight % (wt %) Al_2O_3 particles mixed with SU-8 epoxy were compared. The capacitance increased as the concentration of Al_2O_3 increased, improving the aggregation of the particles (fig. S2). The Al_2O_3 (10%)/SU-8 (90%) composite was an optimal mixture for obtaining a uniform surface and desired capacitance. A sensor was formed at the intersection of the top and bottom electrodes (Fig. 1D). The horseshoe-shaped electrode protected the device from the mechanical stretching that occurred when the device was mounted on the convoluted skin. The sensor capacitance can be affected by sweat and weak electrical conductivity of the skin. To reduce this error, we integrated the two-layer graphene under the substrate of the temperature sensor, which still supports the temperature-sensing capability. In addition, the graphene under the substrate could function as a heater for therapy with static bias current. The total thickness and optical transmittance of this device, including the medical patch used as the substrate, are ~30 μm and ~80%, respectively. The thinner device facilitates good mechanical flexibility and conformable contact with the skin, enabling the precise measurement of the temperature distribution of the skin (fig. S3). In addition, the high optical transparency of the device (~80%) allows direct observation of the attached skin area with the naked eye. Table S1 summarizes the advantages of this device compared to the previously reported wearable thermal sensors.

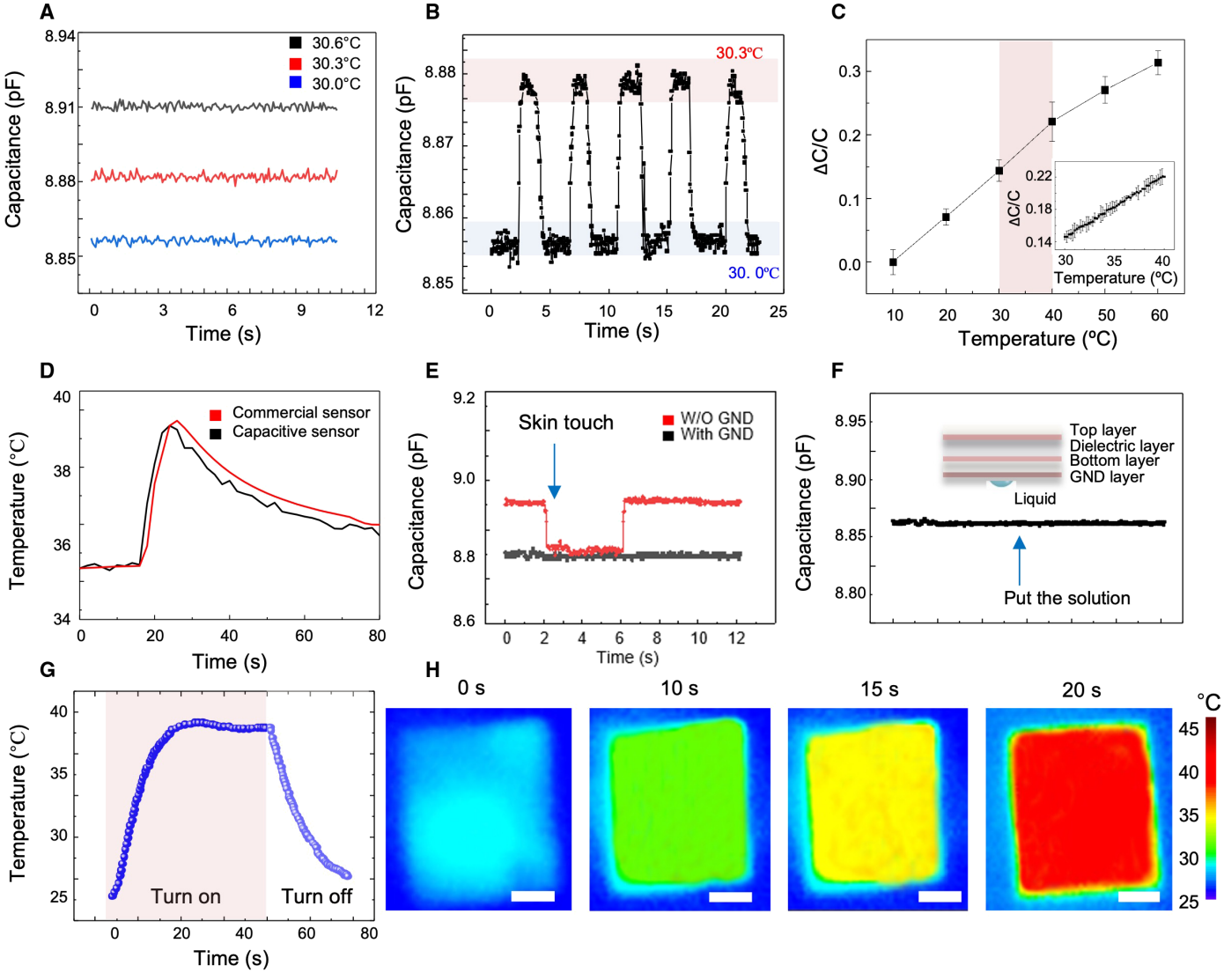

Fig. 2. Functional demonstrations of capacitive temperature sensor patch. (**A**) Capacitance change over temperature variation in three steps (30.0°, 30.3°, and 30.6°C). (**B**) Capacitance change over five cycles at 0.3°C. (**C**) Relative capacitance change with varying temperature (inset: high-resolution measurement in the range from 30° to 40°C). (**D**) Temperature comparison between a commercial sensor and the capacitive sensor. (**E**) Capacitance change using the ground shielding layer for the elimination of noise due to contact with skin. (**F**) Capacitance change using the ground shielding layer. The solution implies sweat on skin. (**G**) Temperature profiles of graphene-based heaters at an input voltage of 5 V. (**H**) IR image captured during the graphene-based heater operation. Scale bar, 1 cm.

The wearable device is connected to a miniaturized FPCB (29 mm by 29 mm), including a readout front end, an analog-to-digital converter (ADC), a microcontroller, an Xtal XO, Bluetooth low energy (BLE), a DC/DC converter, and a battery (Fig. 1E and fig. S4). The readout front end detects the temperature-dependent charge on the sensing capacitor C_S, measured in two phases: Φ_1 and Φ_2, as shown in Fig. 1F. The sampled charge on the C_S is transferred to the integration capacitor C_{INT}, and then the resulting output V_O is converted to digital values via the following ADC. The 8 by 8 channel sensor is configured as a mutual capacitor configuration (fig. S5). A common transmit (TX) driver, which consists of a voltage buffer and a 1-to-8 multiplexer and is synchronized to the readout phase, delivers the sequential pulse of V_{DD} (1.9 V). The sensor output is connected to the readout Integrated Circuit (IC) via an 8-to-1 multiplexer. The switched-capacitor charge integrator on the front end converts the input charge into the voltage signal, and the integrated voltage is digitized by the ADC. By optimizing the Resistance/Capacitance (R/C) parameters in the readout path, the readout enables a conversion time of less than 0.1 s, which is much shorter than the sensor's response time. Owing to the short measurement cycle, the response time to read the capacitance in the system is also short. Last, the measured data from the sensor array are transmitted to a smartphone via the BLE connection.

The graphene-based sensor exhibited a constant and stable capacitance variation from 8.855 to 8.878 pF, as the temperature slightly increased from 30.0° to 30.6°C after the initial calibration (Fig. 2A). During the cycling test, the sensor showed a periodic capacitance change with a fast response time of <0.3 s at a high resolution of 0.3°C (Fig. 2B and fig. S6). In particular, the sensor showed a good linear response with a sensitivity of 40.4 fF/°C in the range of human body temperature (Fig. 2C). Another tendency to change over 40°C may be induced by the thermal expansion of the polymer substrate. As a result, the change in capacitance correlated well with the change in temperature, allowing for data conversion between the two parameters. The data obtained with a graphene-based temperature sensor were compared with that obtained using a commercial medical thermometer (TM-917, Lutron), which can a distinguish temperature change of ~0.01°C. The two data plots showed that the results of the developed sensor are consistent with those of the commercial sensor (Fig. 2D).

Since the capacitive temperature sensor is mounted directly on the skin, it is necessary to isolate it from the noise associated with the skin. The graphene substrate as a ground shielding layer, which was installed at the bottom of the capacitive sensor, effectively reduced the coupling noise (Fig. 2E). Without the ground shielding layer, a slightly conductive skin touching the sensor induced a substantial change in the capacitance. In contrast, the sensor with the ground shielding layer exhibited slight variation. The ground layer reduced the baseline because it could effectively absorb the fringe electric field effectively. The sweat produced by the skin could also act as a noise source. The ground shielding layer effectively inhibited the noise caused by the sweat. When the liquid electrolyte fell to the sensor, an ~2% increase in capacitance was observed (Fig. 2F). In addition to the shielding layer, the graphene layer acted as a heater for thermotherapy and sensor calibration. The heater presents a power efficiency of 0.11 W cm^{-2}, enabling the operation for about 5 hours using a lithium battery with a capacity of 500 mAh. The graphene heater rapidly increased the temperature to 40°C for 20 s, and then the sensor was calibrated. As a result, the thermal sensor array achieved a two-point calibration, the errors of which were zeroed at low and high temperatures of the target range. This two-point calibration improved the accuracy of the temperature measurements from the graphene-based thermal sensor (fig. S7).

To confirm the temperature mapping capability of the sensor array, the (2,2) and (6,7) pixels of the sensor array were locally heated by 2°C using the point heater (Fig. 3A). The sensor immediately reached the maximum temperature after heating up for 2.1 s and

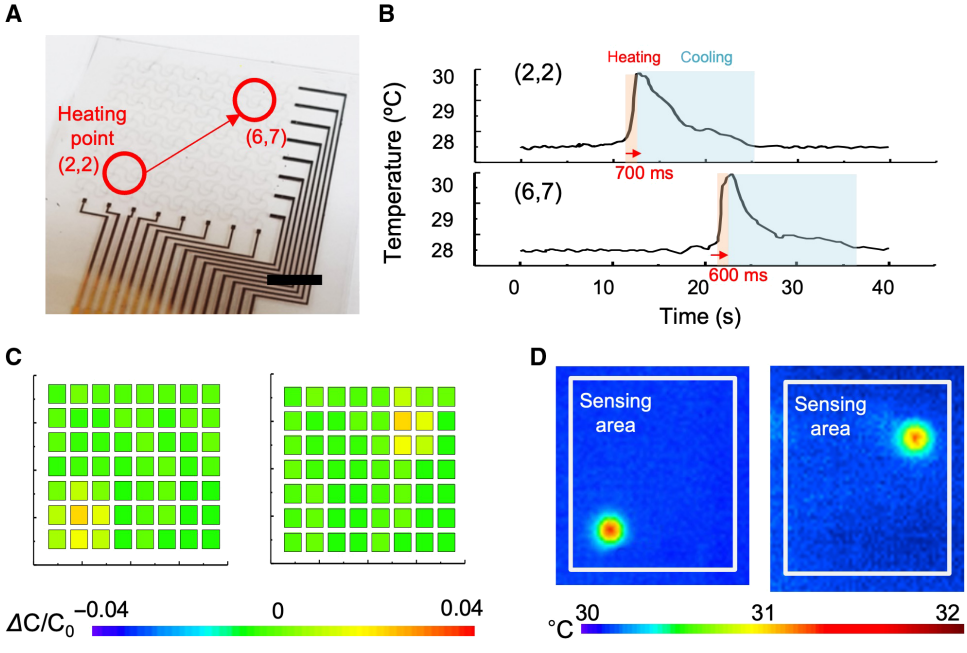

Fig. 3. Performance of temperature sensor array. (**A**) Device configuration for wireless measurement. The heating points start from (2,2) and move to (6,7). Scale bar, 0.5 cm. (**B**) Raw measurement result from the capacitive sensor. (**C**) Capacitance mapping data on the smartphone. (**D**) IR images corresponding to each stage of evaluation.

cooled to the base temperature in 12 s under air conditions (Fig. 3B). The sensor clearly showed hotspots, which were similar to the results of the IR image (Fig. 3C). The device exhibited a spatial resolution of ~2.4 mm according to the design of the sensor array, which can be further improved through the design optimization of sensors (fig. S1). To verify the practical application of the thermal patch, we monitored the change in the skin temperature during various physical activities, such as sleep and exercise. Vigorous exercise increases the skin temperature because a large amount of energy produced by the muscles is converted into heat. In response, sweat is released as a reaction of the nervous system to control the body temperature. The graphene-based temperature sensor attached to the arm monitored the change in the skin temperature during cycling. The measured thermal gradient was transmitted to the smartphone in real time, and the user could conveniently check the data (Fig. 4A and movie S1). In the ready state, the skin temperature was ~30.1°C (the skin temperature near the arm was generally 2° to 10°C lower than the core body temperature), which then increased to 31.4°C as the body movement increased. After the exercise was stopped, the body temperature was retained at the elevated temperature for a certain period of time and gradually returned to its original value under the influence of external temperature and humidity. Eight minutes after the exercise, the body temperature dropped to 30.7°C, and after 35 min, it returned to the initial skin temperature of 30.1°C when the room temperature was 22°C (Fig. 4B). These results are consistent with those from the IR image (Fig. 4C). Moreover, we observed the changes in the skin temperature during sleep. When in a deep sleep, the body temperature reduced as the brain activity decreased. The observation of the body temperature during sleep is significant in detecting sleep disorders. Sleep disorders, such as insomnia, are associated with a decrease in the ability to regulate the body temperature, and the pattern of the sleep disorders can be identified through the changes in the body temperature during sleep (*26*). Therefore, the body temperature using the graphene-based sensor placed in the neck area was monitored in real time during sleep (room temperature, 22°C), which showed the temperature closest to the core body temperature (Fig. 4E and fig. S8). The body temperature during an 8-hour sleep period decreased by ~1.7°C in deep sleep (Fig. 4, F and G). The temperature drop of 1.7°C was associated with a decrease of −0.7% in the capacitance value. The device exhibited stable operation in these long-term experiments without any serious device error and aided in monitoring the changes in temperature during physical activities and/or sleep disorders.

In addition to monitoring the real-time body temperature during physical activities, this sensor is intended to diagnose diseases and perform heat treatments on the attached area. In the human body,

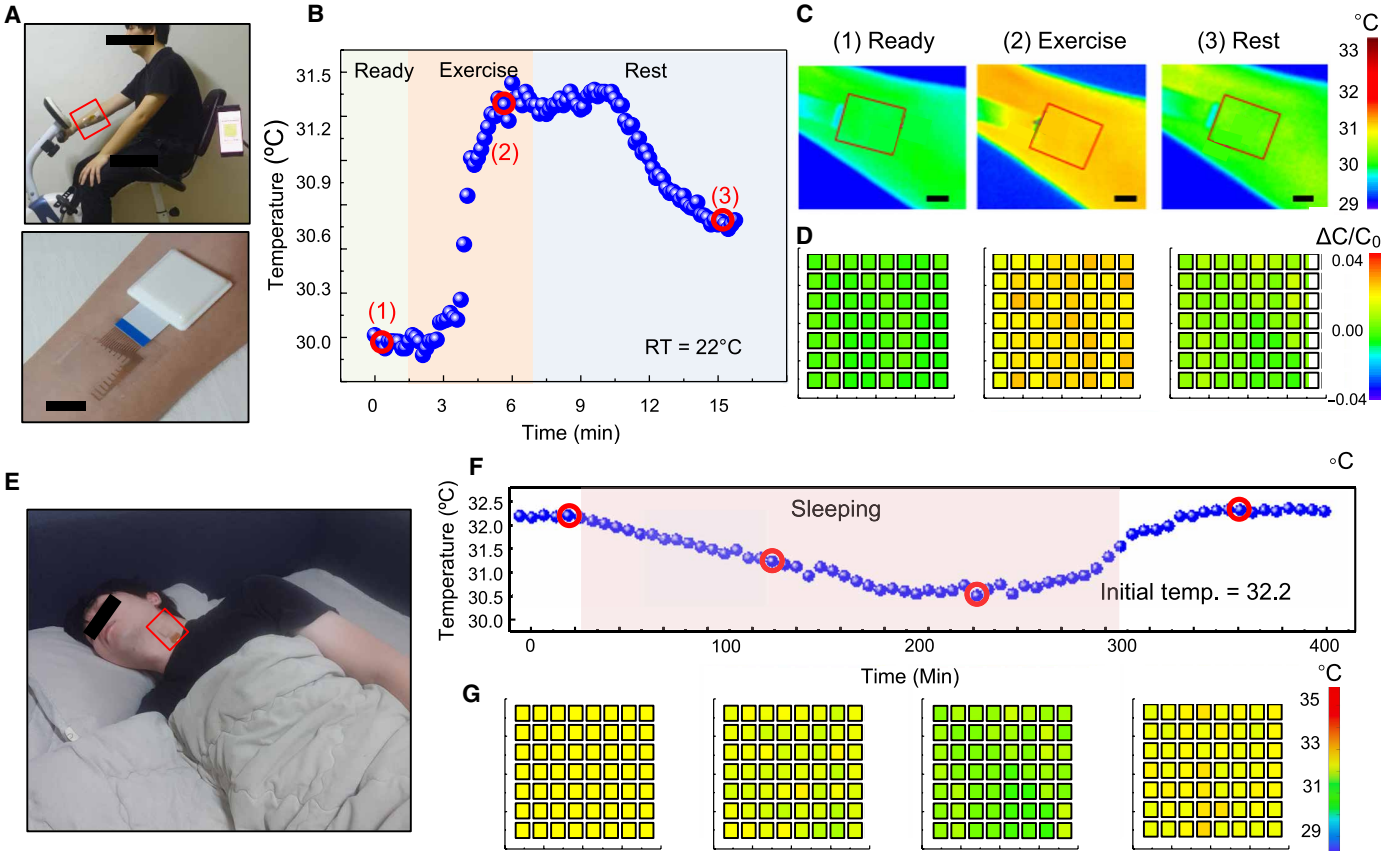

Fig. 4. Practical applications of skin-mounted temperature sensor. (**A**) Device configuration and optical image for wireless measurement. The red box shows the enlarged image of the attached sensor. Scale bars, 2 cm. (**B**) Real-time monitoring using the wireless temperature sensor during exercise. Exercise is divided into three stages: ("ready"), during ("exercise"), and immediately after exercise ("rest"). RT, room temperature. (**C** and **D**) IR images and capacitance mapping for each stage. Each point corresponds to the graph of (B). Scale bar, 1 cm. (**E**) Optical image of the device laminated onto the neck for the measurement during sleep. The inset shows the enlarged image of the attached sensor. (**F**) Long-term monitoring during the sleep. (**G**) Capacitance mapping data during the sleep. Each point corresponds to the red mark in the graph of (G).

the changes in body temperature are expressed according to the supply of blood, and the expression patterns differ according to the type of disease. In existing thermography studies, research on various diseases is generally conducted on the basis of the temperature distribution obtained from the IR images. In general, when an inflammatory reaction or a wound on the skin occurs, the blood flow to the affected area increases, which increases the temperature of the affected area. In the case of a skin tumor, the temperature difference was reported to be greater than 1°C, depending on the type of the skin tumor (*27*). In addition, research on disorders caused by blood circulation imbalance owing to diseases, such as the heart, is being conducted. When an imbalance in blood flow occurs because of complications caused by the deterioration of kidney function, the difference in temperature distribution occurs on the surface of the organ. This factor can be used to determine disease progression (*28*).

To noninvasively diagnose diseases, we developed a rat necrosis model (Fig. 5A). The left renal artery was clamped to induce renal infarction, and the surgical incision was sutured (Fig. 5B). All

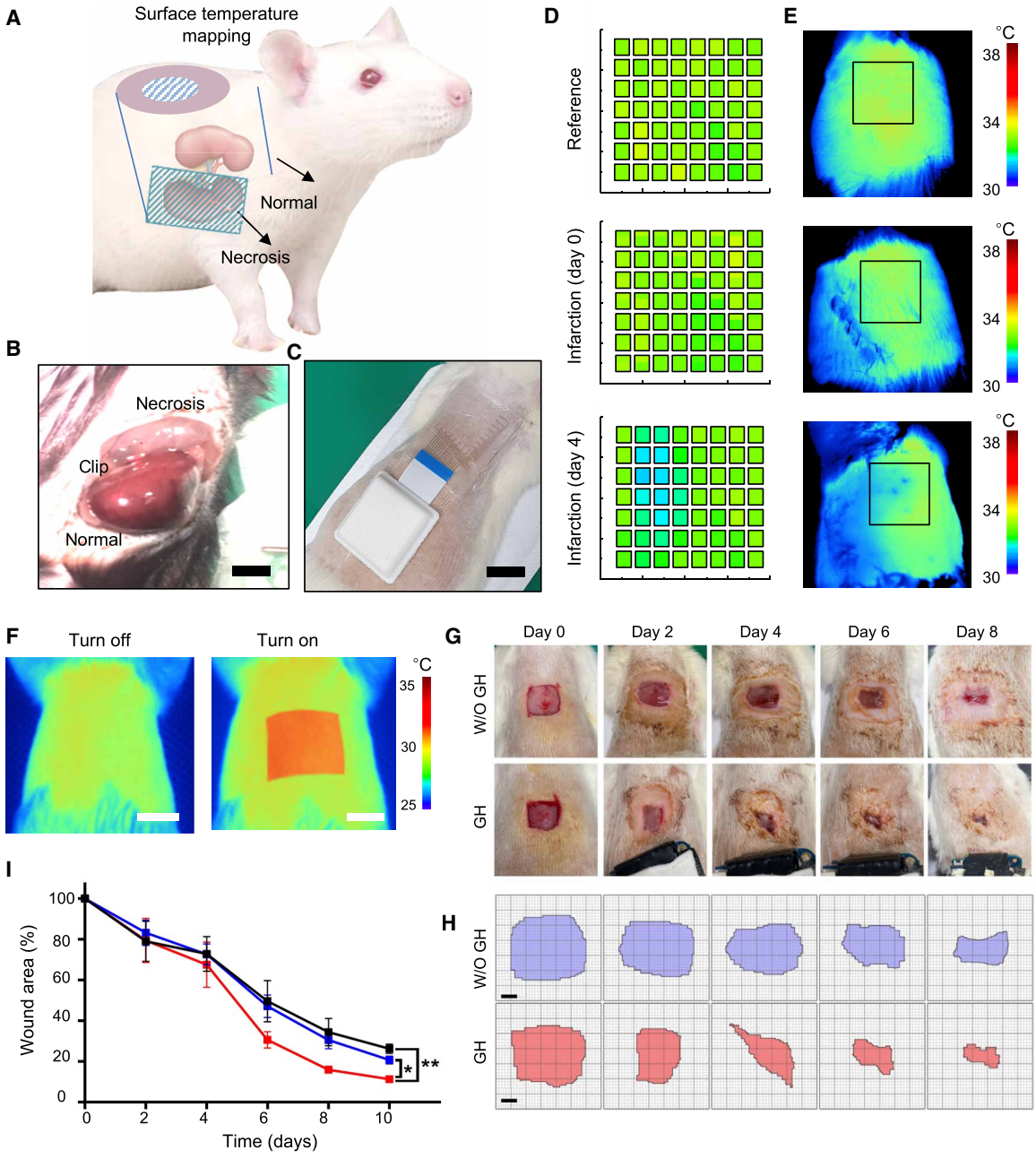

Fig. 5. Animal experiment for diagnosis of diseases and heat treatment. (**A**) Experiment setup for diagnosis of kidney necrosis. (**B**) Optical image of surgery. The blood vessel of the darker kidney is clogged with a clip. Scale bar, 5 mm (**C**) Optical image of the sensor system mounted on the back of the rat. Scale bar, 2 cm. (**D**) Comparison between capacitance mapping and (**E**) IR image for necrosis and sham models. (**F**) IR image of graphene-based heater operation. Scale bars, 1 cm (**G**) Optical images of wound size with and without the graphene heater for 8 days. (**H**) Quantification of wound size based on (G). Scale bars, 2 mm. (**I**) Comparison of the average wound size quantified by area over 10 days for three different groups (control group, W/O GH group, and GH group).

measurements (or data) were remotely obtained using the FPCB connected to the sensor and transmitted directly to the smartphone (Fig. 5C). Rats in three states (control, sham, and necrosis groups; five animals per group) were compared using the temperature mapping results and IR images (Fig. 5, D and E). The temperature of the target area in the sham group rarely changed through the IR images and capacitance mapping. In contrast, 3 days after the necrosis operation, the sensor attached to the surgical site had a temperature 0.7°C lower than that of the surrounding area, as the blood supply to the area decreased (fig. S9). Thus, the temperature sensor can be used to diagnose various diseases, such as renal, heart, brain, and kidney infarctions.

In addition, we conducted an experiment to confirm the thermal therapeutic function of the wearable thermal patch using a rat with a skin wound on the back. Thermotherapy is considered effective in the postacute phase of the skin wound healing. Heat raises the tissue temperature, which causes vasodilation and/or rapid blood pressure, increasing the supply of oxygen and nutrients for healing, and reducing carbon dioxide and metabolic waste in the heated skin area. The graphene heater mounted below the thermal sensor array can increase the temperature up to 3°C with a resolution of approximately 0.2°C for an effective thermal therapy (Fig. 5F). To maintain the optimum temperature, the heater temperature was maintained at 32°C to accelerate the wound healing at the surgical site. The thermotherapeutic effect of the heater for the effective skin regeneration rate was confirmed with three cases—control group (without patch at all), W/O GH group (with patch that is not heated), and GH group (with a graphene heater patched) (fig. S10). As shown in Fig. 5 (G and H), the healing of the wound area was faster in the graphene heater group than in the sham group. Comparing the average wound area of each group over time, it was confirmed that the wounded skin covered with the graphene heater cured approximately 30% smaller than that without a heater on the eighth day of treatment (Fig. 5I and fig. S11). After 14 days, the wound was practically healed with the graphene heater. In contrast, in the case of the rat without a heater, the wound remained up to 14 days. Beyond wound healing, thermotherapy could be widely used in the treatment of various skin diseases, such as skin troubles and skin cancers.

DISCUSSION

In this study, we developed a wearable thermal patch that consists of a capacitive temperature sensor array for temperature mapping and a therapeutic heating system for thermotherapy. This sensor array can continuously monitor temperature during physical activities and help to identify health issues by obtaining the temperature distribution profile of a target area. In addition, a graphene heater mounted under the temperature sensor could increase the healing rate of the injured skin, presumably through vasodilation. These functions have been successfully demonstrated through the monitoring of human and animal experiments. This wearable thermal patch can be useful in bio-healthcare systems with structures and functionalities that cannot be achieved using conventional devices and techniques.

MATERIALS AND METHODS

Fabrication of graphene-based capacitive sensor array

Graphene was grown using CVD on a Cu foil. Subsequently, Cu was etched in ammonium 250 persulfate (20 g dissolved in 1000 ml of deionized water) after coating with poly(methyl methacrylate) as a supporting layer. The fabrication process of the device began by spin-coating a thin film of SU-8 (~3 μm) on a sacrificial layer of Cu foil (fig. S12). The metal interconnects (Cr/Au, 3 nm/35 nm) were defined using lift-off method. Two-layer graphene was transferred and patterned by photolithography for the bottom electrode. As a dielectric layer, SU-8/Al_2O_3 (10 wt %) was coated (3000 rpm) and cured (80°C). Similarly, top electrodes were defined by metal deposition and graphene transfer/patterning. SU-8 layer, which was coated (3000 rpm) and cured, was transferred on to the capacitive sensor for encapsulation. By etching the sacrificial layer, the whole sensor was transferred on a medical patch (20 μm; Tedagram), which already has a three-layer graphene for ground layer. Then, the sensor/heater was bonded to a flexible cable for connection with the FPCB.

Evaluation of animal models

The studies were conducted on 7-week-old male Sprague-Dawley rats for the necrosis model and simple skin wound model. The rats were housed with a 12-hour light-dark cycle, and food and water were provided ad libitum. All protocols were approved by the Institutional Animal Care and Use Committee of Incheon National University, and all experiments were performed according to the relevant guidelines and regulations.

Experimental renal infarction

All animal experiments were verified through a population of five animals. Each group showed relatively consistent data trends. We compared three different groups in this measurement: control group (without any surgery), sham group (laparotomy except infarction), and infraction group (with surgery for infarction). Before the induction of renal infarction, the rats were anesthetized by inhalation of isoflurane vaporized at concentrations of up to 5% in the induction phase and 2% during the surgical procedures. Isoflurane was vaporized in a ratio of 2:1 N_2 and O_2 mixture. Next, the rat's hair in the surgical area was shaved and disinfected with povidone iodine. In the supine position, a small incision on the left side of the abdomen was made using surgical scissors. The kidney was briefly externalized, and the left renal artery was identified. For clipping, a nylon suture was placed under the left renal artery for vessel isolation, and the isolated renal artery was blocked for 30 min using a microvascular clamp (S&T AG, Neuhausen, Switzerland). After clamping, the microvascular clamp was removed, and reperfusion was performed for 5 min. After the reperfusion period, the muscle layer and abdominal skin incision were sutured. No surgical procedures were included in the sham group (control group). The sham group underwent most of the surgical procedures but did not undergo renal infarction.

Wound creation

All animal experiments were verified through a population of five animals. We compared three groups in this experiment: control group (without patch at all), W/O GH group (with patch that is not heated), and GH group (with a graphene heater patched). The rats were anesthetized and shaved. Full-thickness skin wound excision of 1 × 1 cm was performed on the back of each rat and left open. In the wound group without the graphene-based heater (W/O GH), no treatment was used. It was covered with Tegaderm film (Transparent Film Dressing Frame Style, 3M Health Care, USA) and medical tape (3M Soft Cloth Tape with Liner, 3M Health Care, Korea).

It was changed every 12 hours, twice a day. The Tegaderm film was fixed with medical tape and applied under anesthesia. In contrast, in the wound group with the graphene-based heater (GH), the graphene-based heater was used for thermal treatment. The device was fixed to the shaved dorsal skin surface of the rat. The battery of the graphene-based heater was changed every time the Tegaderm film and medical tape were changed. All the wound areas were photographed and measured on days 0, 2, 4, 6, 8, 10, 12, and 14 after wounding.

SUPPLEMENTARY MATERIALS

Supplementary material for this article is available at https://science.org/doi/10.1126/sciadv.abm6693

REFERENCES AND NOTES

1. K. M. Lovett, B. A. Liang, Risks of online advertisement of direct-to-consumer thermography for breast cancer screening. *Nat. Rev. Cancer* **11**, 827–828 (2011).
2. Y. S. Oh, J.-H. Kim, Z. Xie, S. Cho, H. Han, S. W. Jeon, M. Park, M. Namkoong, R. Avila, Z. Song, S.-U. Lee, K. Ko, J. Lee, J.-S. Lee, W. G. Min, B.-J. Lee, M. Choi, H. U. Chung, J. Kim, M. Han, J. Koo, Y. S. Choi, S. S. Kwak, S. B. Kim, J. Kim, J. Choi, C.-M. Kang, J. U. Kim, K. Kwon, S. M. Won, J. M. Baek, Y. Lee, S. Y. Kim, W. Lu, A. Vazquez-Guardado, H. Jeong, H. Ryu, G. Lee, K. Kim, S. Kim, M. S. Kim, J. Choi, D. Y. Choi, Q. Yang, H. Zhao, W. Bai, H. Jang, Y. Yu, J. Lim, X. Guo, B. H. Kim, S. Jeon, C. Davies, A. Banks, H. J. Sung, Y. Huang, I. Park, J. A. Rogers, Battery-free, wireless soft sensors for continuous multi-site measurements of pressure and temperature from patients at risk for pressure injuries. *Nat. Commun.* **12**, 5008 (2021).
3. B. B. Lahiri, S. Bagavathiappan, T. Jayakumar, J. Philip, Medical applications of infrared thermography: A review. *Infrared Phys. Technol.* **55**, 221–235 (2012).
4. M. Kang, J. Kim, B. Jang, Y. Chae, J.-H. Kim, J.-H. Ahn, Graphene-based three-dimensional capacitive touch sensor for wearable electronics. *ACS Nano* **11**, 7950–7957 (2017).
5. C. Tan, Z. Dong, Y. Li, H. Zhao, X. Huang, Z. Zhou, J.-W. Jiang, Y.-Z. Long, P. Jiang, T.-Y. Zhang, B. Sun, A high performance wearable strain sensor with advanced thermal management for motion monitoring. *Nat. Commun.* **11**, 3530 (2020).
6. H. Fang, K. J. Yu, C. Gloschat, Z. Yang, E. Song, C.-H. Chiang, J. Zhao, S. M. Won, S. Xu, M. Trumpis, Y. Zhong, S. W. Han, Y. Xue, D. Xu, S. W. Choi, G. Cauwenberghs, M. Kay, Y. Huang, J. Viventi, I. R. Efimov, J. A. Rogers, Capacitively coupled arrays of multiplexed flexible silicon transistors for long-term cardiac electrophysiology. *Nat. Biomed. Eng.* **1**, 0038 (2017).
7. Y. Wang, S. Lee, T. Yokota, H. Wang, Z. Jiang, J. Wang, M. Koizumi, T. Someya, A durable nanomesh on-skin strain gauge for natural skin motion monitoring with minimum mechanical constraints. *Sci. Adv.* **6**, eabb7043 (2020).
8. S. Han, J. Kim, M. Won Sang, Y. Ma, D. Kang, Z. Xie, K.-T. Lee, U. Chung Ha, A. Banks, S. Min, Y. Heo Seung, R. Davies Charles, W. Lee Jung, C.-H. Lee, H. Kim Bong, K. Li, Y. Zhou, C. Wei, X. Feng, Y. Huang, J. A. Rogers, Battery-free, wireless sensors for full-body pressure and temperature mapping. *Sci. Transl. Med.* **10**, eaan4950 (2018).
9. J. Kim, M. Lee, H. J. Shim, R. Ghaffari, H. R. Cho, D. Son, Y. H. Jung, M. Soh, C. Choi, S. Jung, K. Chu, D. Jeon, S.-T. Lee, J. H. Kim, S. H. Choi, T. Hyeon, D.-H. Kim, Stretchable silicon nanoribbon electronics for skin prosthesis. *Nat. Commun.* **5**, 5747 (2014).
10. T. Q. Trung, H. S. Le, T. M. L. Dang, S. Ju, S. Y. Park, N.-E. Lee, Freestanding, fiber-based, wearable temperature sensor with tunable thermal index for healthcare monitoring. *Adv. Healthc. Mater.* **7**, 1800074 (2018).
11. C. Yan, J. Wang, P. S. Lee, Stretchable graphene thermistor with tunable thermal index. *ACS Nano* **9**, 2130–2137 (2015).
12. R. C. Webb, A. P. Bonifas, A. Behnaz, Y. Zhang, K. J. Yu, H. Cheng, M. Shi, Z. Bian, Z. Liu, Y.-S. Kim, W.-H. Yeo, J. S. Park, J. Song, Y. Li, Y. Huang, A. M. Gorbach, J. A. Rogers, Ultrathin conformal devices for precise and continuous thermal characterization of human skin. *Nat. Mater.* **12**, 938–944 (2013).
13. T. Yokota, Y. Inoue, Y. Terakawa, J. Reeder, M. Kaltenbrunner, T. Ware, K. Yang, K. Mabuchi, T. Murakawa, M. Sekino, W. Voit, T. Sekitani, T. Someya, Ultraflexible, large-area, physiological temperature sensors for multipoint measurements. *Proc. Natl. Acad. Sci. U.S.A.* **112**, 14533–14538 (2015).
14. Q. Trung, T. M. L. Dang, S. Ramasundaram, P. T. Toi, S. Y. Park, N.-E. Lee, A stretchable strain-insensitive temperature sensor based on free-standing elastomeric composite fibers for on-body monitoring of skin temperature. *ACS Appl. Mater. Interfaces* **11**, 2317–2327 (2019).
15. J. Jeon, H.-R. Lee, Z. Bao, Flexible wireless temperature sensors based on Ni microparticle-filled binary polymer composites. *Adv. Mater.* **25**, 850–855 (2013).
16. Q. Lyu, S. Gong, J. Yin, J. M. Dyson, W. Cheng, Soft wearable healthcare materials and devices. *Adv. Healthc. Mater.* **10**, 2100577 (2021).
17. H. Park, W. Park, C. H. Lee, Electrochemically active materials and wearable biosensors for the in situ analysis of body fluids for human healthcare. *NPG Asia Mater.* **13**, 23 (2021).
18. S. Choi, J. Park, W. Hyun, J. Kim, J. Kim, Y. B. Lee, C. Song, H. J. Hwang, J. H. Kim, T. Hyeon, D.-H. Kim, Stretchable heater using ligand-exchanged silver nanowire nanocomposite for wearable articular thermotherapy. *ACS Nano* **9**, 6626–6633 (2015).
19. S.-H. Ha, J.-M. Kim, Rapid and economic preparation of wearable thermotherapy pad based on simple cut-patterning of metal foil supported by plastic sheets. *RSC Adv.* **11**, 918–926 (2021).
20. M. Dehghan, F. Farahbod, The efficacy of thermotherapy and cryotherapy on pain relief in patients with acute low back pain, a clinical trial study. *J. Clin. Diagn. Res.* **8**, LC01–LC04 (2014).
21. T. Ikeda, F. Tayefeh, D. I. Sessler, A. Kurz, O. Plattner, B. Petschnigg, H. W. Hopf, J. West, Local radiant heating increases subcutaneous oxygen tension. *Am. J. Surg.* **175**, 33–37 (1998).
22. A. A. Khan, P. E. Banwell, M. C. Bakker, P. G. Gillespie, D. A. McGrouther, A. H. N. Roberts, Topical radiant heating in wound healing: An experimental study in a donor site wound model. *Int. Wound J.* **1**, 233–240 (2004).
23. S. Bae, H. Kim, Y. Lee, X. Xu, J.-S. Park, Y. Zheng, J. Balakrishnan, T. Lei, H. Ri Kim, Y. I. Song, Y.-J. Kim, K. S. Kim, B. Özyilmaz, J.-H. Ahn, B. H. Hong, S. Iijima, Roll-to-roll production of 30-inch graphene films for transparent electrodes. *Nat. Nanotechnol.* **5**, 574–578 (2010).
24. Y. J. Park, S.-K. Lee, M.-S. Kim, H. Kim, J.-H. Ahn, Graphene-based conformal devices. *ACS Nano* **8**, 7655–7662 (2014).
25. Q. Wu, Y. Qiao, R. Guo, S. Naveed, T. Hirtz, X. Li, Y. Fu, Y. Wei, G. Deng, Y. Yang, X. Wu, T.-L. Ren, Triode-mimicking graphene pressure sensor with positive resistance variation for physiology and motion monitoring. *ACS Nano* **14**, 10104–10114 (2020).
26. L. Lan, Z. W. Lian, Y. B. Lin, Comfortably cool bedroom environment during the initial phase of the sleeping period delays the onset of sleep in summer. *Build. Environ.* **103**, 36–43 (2016).
27. J. P. Agnelli, A. A. Barrea, C. V. Turner, Tumor location and parameter estimation by thermography. *Math. Comput. Model.* **53**, 1527–1534 (2011).
28. S. Sivanandam, M. Anburajan, B. Venkatraman, M. Menaka, D. Sharath, Medical thermography: A diagnostic approach for type 2 diabetes based on non-contact infrared thermal imaging. *Endocrine* **42**, 343–351 (2012).

Acknowledgments

Funding: This work was supported by the National Research Foundation of Korea (NRF) funded by the Korean government (MSIT) (NRF-2015R1A3A2066337) and the Technology Innovation Program (20012355, fully implantable closed-loop Brain to X for voice communication) funded by MOTIE. S.Y. acknowledges High Risk, High Return Research Program (2020) in the Incheon National University. **Author contributions:** J.-H.A. planned and supervised the project. M.K. conducted most of the experiments regarding the device fabrication and characterizations. H.J. and S.W.P. conducted the animal experiments. J.H. and H.L. designed the circuit and fabricated the array devices. J.-H.A., Y.C., and S.Y. analyzed the data and wrote the manuscript. **Competing interests:** M.K. and J.-H.A. are inventors on a provisional patent application related to this work filed at the Korean Intellectual Property Office (no. 1022756140000, filed 09 July 2021). The authors declare that they have no other competing interests. **Data and materials availability:** All data needed to evaluate the conclusions in the paper are present in the paper and/or the Supplementary Materials.

Submitted 3 October 2021
Accepted 23 February 2022
Published 13 April 2022
10.1126/sciadv.abm6693